

# Conformational Changes in the Multidrug Transporter EmrE Associated with Substrate Binding

Christopher G. Tate\*, Iban Ubarretxena-Belandia and Joy M. Baldwin

MRC Laboratory of Molecular Biology, Hills Road, Cambridge CB2 2QH, UK

EmrE is a bacterial multidrug transporter of the small multidrug resistance family, which extrudes large hydrophobic cations such as tetraphenylphosphonium (TPP<sup>+</sup>) out of the cell by a proton antiport mechanism. Binding measurements were performed on purified EmrE solubilized in dodecylmaltoside to determine the stoichiometry of TPP<sup>+</sup> binding; the data showed that one TPP<sup>+</sup> molecule bound per EmrE dimer. Reconstitution of purified EmrE at low lipid:protein ratios in either the presence or the absence of TPP<sup>+</sup> produced well ordered two-dimensional crystals. Electron cryo-microscopy was used to collect images of frozen hydrated EmrE crystals and projection maps were determined by image processing to 7 Å resolution. An average native EmrE projection structure was calculated from the *c*222 and *p*222<sub>1</sub> crystals, which was subsequently subtracted from the average of two independent *p*2 projection maps of EmrE with TPP<sup>+</sup> bound. The interpretation of the difference density image most consistent with biochemical data suggested that TPP<sup>+</sup> bound at the monomer–monomer interface in the centre of the EmrE dimer, and resulted in the movement of at least one transmembrane  $\alpha$ -helix.

© 2003 Elsevier Ltd. All rights reserved.

**Keywords:** electron crystallography; membrane protein; structure; multidrug resistance

\*Corresponding author

## Introduction

Multidrug transporters are characterised by their ability to transport toxins of widely different structures, sizes and, sometimes, charge.<sup>1</sup> The *Escherichia coli* multidrug resistance protein EmrE belongs to the small multidrug resistance (SMR) family of transporters.<sup>2</sup> These transporters all contain about 100–110 amino acid residues that are predicted by hydropathy profiles to form four  $\alpha$ -helical transmembrane domains.<sup>3</sup> Biophysical evidence supporting this four-helix model comes from FTIR studies on EmrE in organic solvents and lipid bilayers<sup>4</sup> and heteronuclear NMR in organic solvents.<sup>5</sup> The projection structure of EmrE at 7 Å resolution confirmed the presence of four transmembrane  $\alpha$ -helices and that they were

organised into a minimal functional unit that was a dimer.<sup>6</sup> The striking feature of this dimer was that in projection it appeared asymmetric, suggesting that the two EmrE monomers could have different conformations. Biochemical analysis, such as negative dominance studies, substrate-binding assays, cross-linking and hybrid oligomerization, all conclude that EmrE functions as an oligomer.<sup>7–10</sup>

The mechanism of drug transport by EmrE has been the subject of many studies. All compounds transported by EmrE are large hydrophobic cations, such as tetraphenylphosphonium (TPP<sup>+</sup>) and ethidium.<sup>11</sup> These compounds are extruded from the cell by an antiport mechanism that uses at least two protons per molecule of toxin transported.<sup>12</sup> On each polypeptide there is only a single charged amino acid residue, Glu14, that is predicted to lie in the centre of a transmembrane domain. Glu14 is essential for the transport mechanism; mutation of Glu14 to any amino acid residue apart from Asp abolishes transport, and the Asp mutant has severely impaired transport

Abbreviations used: TPP<sup>+</sup>, tetraphenylphosphonium; SMR, small multidrug resistance; DDM, dodecylmaltoside; cryo-EM, electron cryo-microscopy.

E-mail address of the corresponding author: cgt@mrc-lmb.cam.ac.uk

kinetics.<sup>13,14</sup> It was proposed that, in the EmrE oligomer, the Glu14 residues in their unprotonated form are involved in the binding of the toxin, and that the protons bind directly to them to cause release of the toxin at the periplasmic surface.<sup>15,16</sup> An analysis of the accessibility of membrane permeant and impermeant maleimides to Cys residues introduced throughout EmrE was used to infer that the pathway in EmrE through which toxins are translocated is predominantly hydrophobic in character.<sup>17,18</sup> We have used electron crystallography of 2D EmrE crystals to identify the conformational changes associated with substrate binding and to locate the probable substrate-binding pocket at the interface between monomers within the EmrE dimer.

## Results and Discussion

### [<sup>3</sup>H]TPP<sup>+</sup> binding assays

The projection structure of EmrE at 7 Å resolution clearly defined the minimal functional unit of EmrE as a dimer.<sup>6</sup> A previous determination of the stoichiometry of TPP<sup>+</sup> bound to EmrE was 1:3,<sup>8</sup> which did not make sense in view of the dimeric structure of EmrE. To clarify this inconsistency, we performed [<sup>3</sup>H]TPP<sup>+</sup> saturation binding assays on purified EmrE solubilized in dodecylmaltoside (DDM). Although TPP<sup>+</sup> is a substrate of EmrE that can be transported across the membrane, at alkaline pH the off-rate is sufficiently slow to allow binding to be measured.<sup>8</sup> The ratio of TPP<sup>+</sup> bound per EmrE monomer was determined from the  $B_{\max}$  value calculated by non-linear regression analysis of the TPP<sup>+</sup> binding data and the concentration of purified EmrE was determined from a colorimetric protein assay that had been calibrated by amino acid analysis (see Materials and Methods). The requirement for 100% functional EmrE in this analysis prevented the use of 2D EmrE crystals, because during crystallisation a proportion of the EmrE invariably aggregated in a presumably inactive state; it was not possible to remove these aggregates efficiently by centrifugation through sucrose density-gradients (C. G. Tate., unpublished results).

Saturation binding assays of purified EmrE solubilized in DDM (Figure 1(a)) gave an apparent  $K_d$  of  $2.6(\pm 0.4)$  nM ( $n = 3$ ), but the ratio of EmrE:TPP<sup>+</sup> varied between 3:1 and 5:1. This variability correlated with the concentration of EmrE in the binding assay; the lower the concentration of EmrE, the closer the ratio was to 5:1. One explanation for these results was that the EmrE dimer was dissociating at the nanomolar concentrations used in the saturation binding assays and concomitantly losing the ability to bind TPP<sup>+</sup>. Analytical ultracentrifugation supports this hypothesis by showing that EmrE in DDM exists as a monomer–dimer equilibrium (P. J. G. Butler & C. G. Tate, unpublished results). Binding assays

were therefore performed with micromolar concentrations of EmrE. At 6.6 μM EmrE, the EmrE:TPP<sup>+</sup> ratio was 2.6, at 15.4 μM EmrE the ratio was 2.3 and at 80.5 μM EmrE the ratio was 1.9 (Figure 1(b)). In these assays, it was necessary to plot total TPP<sup>+</sup> concentration on the  $x$ -axis rather than the free TPP<sup>+</sup> concentration and the ratio of TPP<sup>+</sup>:EmrE was determined from the intersection of the two linear sections of the plot (Figure 1(c)). At low concentrations of TPP<sup>+</sup> virtually all the TPP<sup>+</sup> was bound to EmrE because the TPP<sup>+</sup> concentration was 1000-fold above the apparent  $K_d$  for TPP<sup>+</sup> binding, leading to this section of the graph being linear with a slope of 1; when the concentration of TPP<sup>+</sup> was high, binding to EmrE is saturated and the graph plateaus. The binding data revealed that the stoichiometry of binding was one molecule of TPP<sup>+</sup> per EmrE dimer.

### Projection structures of EmrE with TPP<sup>+</sup> bound

The purification and crystallisation of EmrE was performed as described,<sup>6</sup> except that the crystallisations were performed at higher concentrations of EmrE (1 mg/ml). This led to large 2D crystals 1–2 μm wide and up to 10 μm long. The crystals were flash-frozen in liquid ethane and high-resolution images were collected by electron cryo-microscopy (cryo-EM). Image analysis of the crystals showed that they had  $c222$  plane group symmetry that yielded an EmrE projection map (Figure 2(a)) at 7 Å resolution with good phase residuals (Table 1). Despite the different symmetry from the previously published  $p222_1$  crystal form,<sup>6</sup> the projection maps of the EmrE dimer were virtually identical. The different crystal forms arose through different packing of the crystallographic tetramers, coloured red and blue in Figure 2. Interactions between the tetramers coloured blue are conserved between the  $c222$  and  $p222_1$  crystal forms, but the interactions between the blue and red tetramers differed, creating a 2-fold screw axis in the plane of the membrane in the  $p222_1$  crystal and a 2-fold axis in the plane of the membrane in the  $c222$  crystal.

To obtain 2D EmrE crystals with bound substrate, trials were made of soaking the native EmrE  $c222$  crystals at pH 7 (the pH of crystallisation) in the presence of the substrates TPP<sup>+</sup>, ethidium or acriflavine. EmrE in the 2D crystals was capable of binding substrates as determined by [<sup>3</sup>H]TPP<sup>+</sup> saturation binding analysis (our unpublished results). The samples were subsequently placed onto electron microscope grids and flash-frozen in liquid ethane for analysis by cryo-EM. The addition of either TPP<sup>+</sup> or ethidium induced fragmentation of the crystals as observed at low magnification on the electron microscope, with the ethidium-treated sample being significantly more disordered than the TPP<sup>+</sup>-treated sample. No crystals were seen after treatment with acriflavine. Cryo-EM was used to collect images of the TPP<sup>+</sup>- and ethidium-treated  $c222$

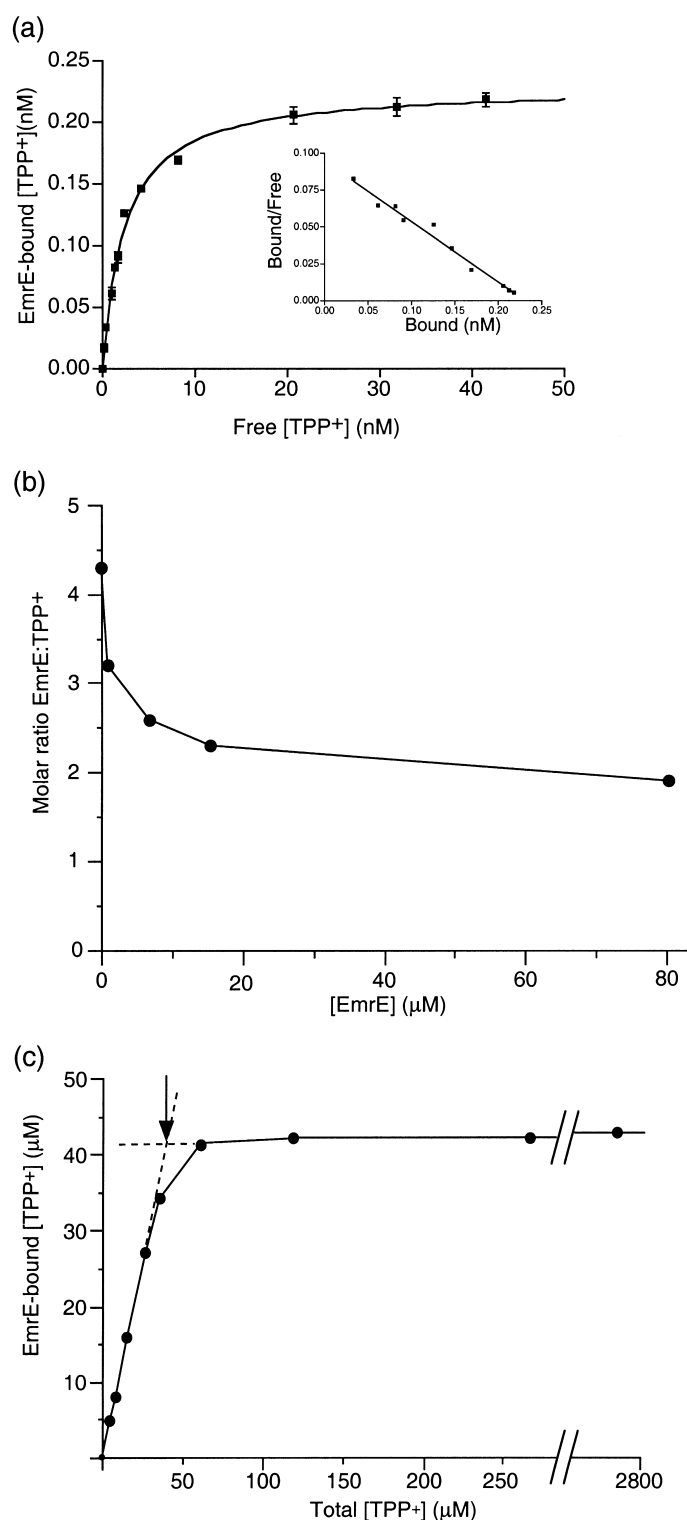


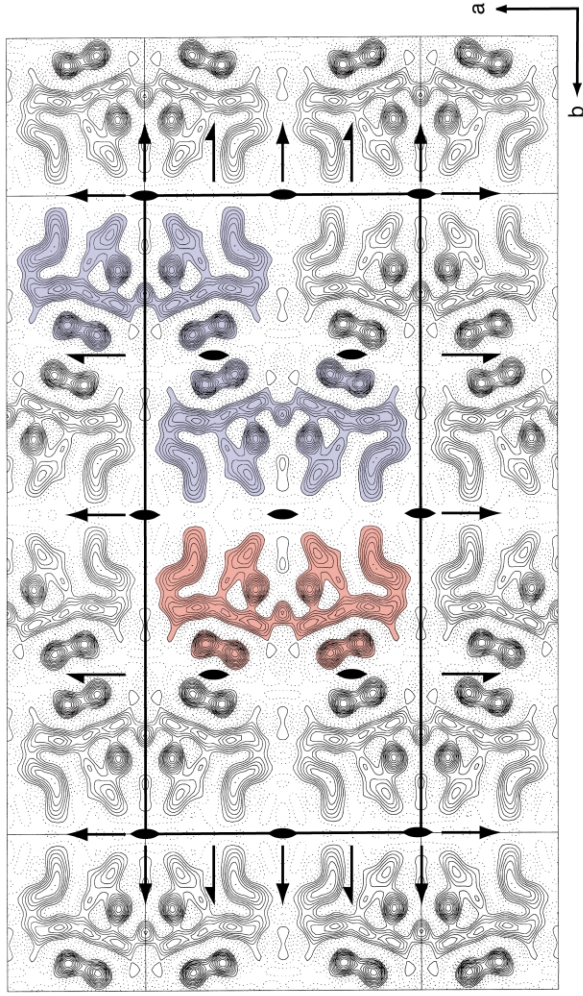
**Figure 1.** Ligand-binding assays on detergent-solubilized EmrE. (a) A saturation binding experiment was performed using a final concentration of 1.5 nM EmrE. Each point was determined in duplicate and the error bars (standard error) are sometimes smaller than the symbol. The data were analysed by non-linear regression to determine  $K_d$  and  $B_{max}$  values. The quality of a single high-affinity binding site are evident from the Scatchard plot (inset). (b) Variation of the EmrE:TPP<sup>+</sup> ratio in relation to the concentration of EmrE in the binding assay. Each point represents the EmrE:TPP<sup>+</sup> ratio determined from a single experiment performed in duplicate. (c) Binding of [<sup>3</sup>H]TPP<sup>+</sup> to a high concentration of EmrE was determined as above, but the conditions of the experiment ensured that the amount of EmrE was greater than [<sup>3</sup>H]TPP<sup>+</sup> for half of the data points. A representative experiment is shown performed in duplicate with a final concentration of 80.5 μM EmrE. Note that the values on the x-axis are of the total TPP<sup>+</sup> concentration and not the free concentration. Extrapolation of the linear portions of the graph are shown in broken lines and the point of inflection used to calculate the TPP:EmrE ratio is shown by an arrow.

crystals. Optical diffraction of the images showed only low-resolution diffraction spots that were very fuzzy, indicating that the *c*222 crystalline lattice had been altered significantly on addition of EmrE substrates, presumably because of substrate-induced conformational changes in EmrE. A single image of a TPP<sup>+</sup>-treated *c*222 crystal was, however, sufficiently good to allow indexing of the diffraction spots after Fourier transformation

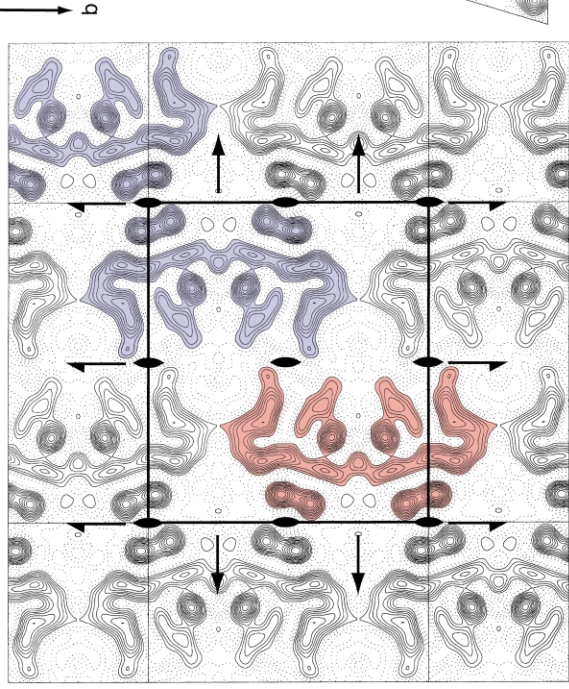
of the digitised image. The only possible indexing gave a plane group symmetry of *p*2, confirming that significant substrate-induced conformational changes in EmrE had occurred. However, the lattice was poorly ordered, with information to only 9 Å resolution.

In order to obtain EmrE crystals with substrate bound, crystallisation in the presence of TPP<sup>+</sup> was necessary. The crystallisation conditions that

(a) c222; native



(b) p222<sub>1</sub>; native



(c) p2; bound TPP+

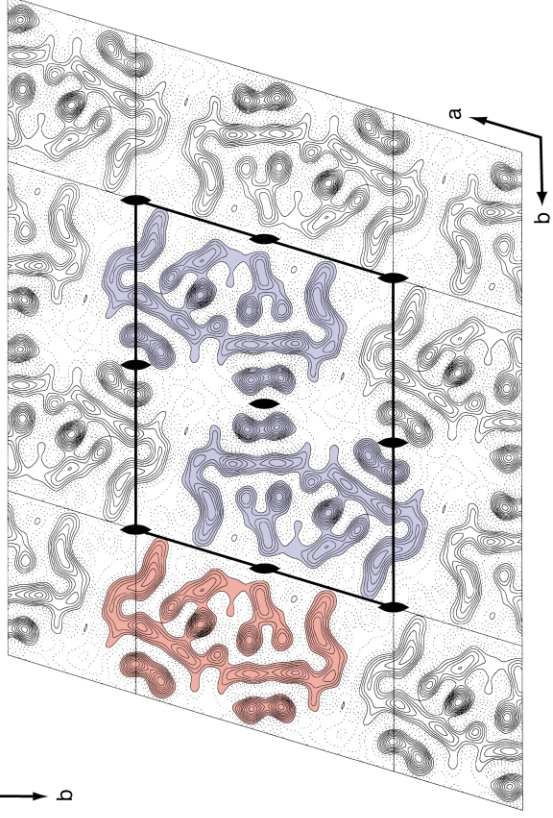


**Table 1.** Electron crystallographic data

	<i>p</i> 2 (data A)	<i>p</i> 2 (data B)	<i>c</i> 222	<i>p</i> 222 <sub>1</sub>				
Plane group symmetry	<i>p</i> 2 (data A)	<i>p</i> 2 (data B)	<i>c</i> 222	<i>p</i> 222 <sub>1</sub>				
Unit cell dimensions								
<i>a</i> (Å)	71.18 ± 0.14	72.33 ± 0.23	72.58 ± 0.28	84.44 ± 0.78				
<i>b</i> (Å)	86.69 ± 0.38	87.62 ± 0.45	166.99 ± 2.02	73.85 ± 0.28				
γ (deg.)	106.98 ± 0.53	107.00 ± 0.60	90.0 ± 0.83	90.0 ± 0.5				
No. images	10	12	6	8				
Range of defocus (Å)	5310–13,504	5601–10,822	6847–10,656	2260–9234				
No. unique reflections to 7 Å	209	173	105	107				
Total observations to 7 Å	1408	1521	914	684				
Overall phase residual to 7 Å (random = 90°)	21.0°	22.7°	19.9°	27.5°				
Temperature factor <i>B</i> <sub>xy</sub> <sup>a</sup> (Å <sup>2</sup> )	437 ± 49	375 ± 43	426 ± 51	339 ± 11				
Resolution range (Å)	No. unique reflections	Phase residual <sup>b</sup>						
200–12.0	74	5.5	71	8.3	43	8.1	45	11.9°
12.0–9.5	37	4.4	34	12.8	17	11.9	22	11.8°
9.5–8.2	32	13.6	34	17.5	23	13.5	20	19.0°
8.2–6.9	55	17.6	52	18.0	30	12.7	30	16.7°
6.9–6.3	38	27.9	33	23.2	19	17.9	20	30.7°
6.3–5.7	48	39.5	48	31.6	20	30.7	31	38.1°

<sup>a</sup> Restores high-resolution contrast by correction for in-plane amplitude fall-off.  
<sup>b</sup> 45° random.

yielded good crystals were identical with those that produced the *c*222 and *p*222<sub>1</sub> crystal forms, except that the pH was 7.5 instead of 7. The morphology of the crystals grown in the presence of TPP<sup>+</sup> was significantly different from the *c*222 and *p*222<sub>1</sub> crystals, in that they were long (~15 μm) flattened tubes that were only about 0.4 μm wide. The EmrE-TPP<sup>+</sup> crystals were flash-frozen in liquid ethane and high-resolution images were collected by cryo-EM. The crystals were well ordered and yielded a 7 Å resolution projection map (Figure 2(c)) of good quality (Table 1). The crystals were of *p*2 symmetry with cell dimensions similar to those of the *p*2 crystal generated by soaking *c*222 crystal with TPP<sup>+</sup> (results not shown), suggesting that the higher pH required to grow the *p*2 crystals played no role in the TPP<sup>+</sup>-induced conformation change. The *p*2 crystal contained a crystallographic tetramer that was superimposable with the equivalent tetramers in the *c*222 and *p*222<sub>1</sub> crystal forms. In addition, the packing characteristics of the crystallographic tetramer were conserved except for the packing along the interface between the red and blue tetramers shown in Figure 2.

The similarity of the crystallographic tetramers

between native EmrE (no TPP<sup>+</sup> bound, *c*222 and *p*222<sub>1</sub> crystal forms) and EmrE with TPP<sup>+</sup> bound (*p*2 crystal form) suggested that there were no gross changes in EmrE structure upon substrate binding, but there were small differences in detail visible in the maps that could be significant. The aim was to calculate a difference map between the native and TPP<sup>+</sup>-bound forms of EmrE, but this was problematic because the three projection maps had three different plane group symmetries. It was therefore not possible to create difference maps as has been previously performed in, for example, the analysis of conformation changes in bacteriorhodopsin;<sup>19</sup> in this case, the symmetry of the crystals was unchanged and difference maps were created simply by the subtraction of the amplitudes in Fourier space and re-projection of the difference map in real space. The only way to average or subtract the projection maps of EmrE was to use the density map from the real space image, in a manner analogous to single-particle image processing. It was predicted that this would result in noisier difference images than if the difference map was made by the subtraction of amplitudes. We therefore determined another projection map of EmrE with TPP<sup>+</sup> bound from an

**Figure 2.** Projection maps of EmrE at 7 Å resolution. The crystallographic data for each of the projection maps are shown in Table 1. The *p*222<sub>1</sub> projection map was described by Tate *et al.*<sup>6</sup> A single unit cell is shown for each projection map with its symmetry elements: ovals, 2-fold axes perpendicular to the membrane; half arrows, screw axes in the plane of the membrane; arrows, 2-fold axes in the plane of the membrane. The *a* and *b* axes are indicated for each unit cell at the corner of the maps. The *c*222 and *p*222<sub>1</sub> crystals did not contain any added substrate, but the *p*2 crystal contained the substrate TPP<sup>+</sup>. The packing arrangement is shown by the coloured crystallographic tetramers; packing interactions between blue tetramers are conserved in all the crystal forms, but the interactions between red and blue tetramers vary.

**Table 2.** Unit cell dimensions after optimisation and scaling

Unit cell parameters	<i>c</i> 222	<i>p</i> 222 <sub>1</sub>			<i>p</i> 2:A			<i>p</i> 2:B		
	Fixed	Exp	72.5	Opt	Exp	72.5	Opt	Exp	72.5	Opt
<i>a</i> (Å)	72.5	84.0	82.3	84.25	71.0	72.5	72.5	72.3	72.5	72.5
<i>b</i> (Å)	167.0	74.0	72.5	72.5	86.5	88.3	85.75	87.6	91.8	85.75
$\gamma$ (deg.)	90.0	90.0	90.0	90.0	107.0	107.0	107.0	107.0	107.0	107.0
Scale factor	1.0	–	–	1.0	–	–	1.0	–	–	0.9

Exp, unit cell dimensions determined experimentally; 72.5, unit cell dimensions after altering the unit cell dimension parallel with the rows of (blue) tetramers to 72.5 Å; Opt, unit cell dimensions after optimisation to reduce the rms density difference between the projection maps.

independent purification and crystallisation experiment (Table 1) with the expectation that any alterations in the density distribution conserved between the different images would be the most important biological changes caused by substrate binding.

### Construction of difference images

The first step in the analysis of the projection maps was to create a gallery of images aligned to a grid with standardized cell dimensions. This was essential because there were small differences in magnification between the different projection maps that gave rise to large density differences unrelated to substrate binding when they were compared (our unpublished results). The individual cell dimensions and density scale factor were optimised (Table 2) by a search procedure to minimise the root-mean-square (rms) density differences between masked crystallographic tetramers (see Materials and Methods). The improvement after the search process is seen as a clear reduction in the rms density difference between images (Table 3). It was found empirically that the cell dimensions had to be varied independently of each other for accurate comparisons between the density maps, although the reason why anisotropic scaling was required is unclear. The density maps calculated with the optimised parameters were averaged without any loss of structural features (Figure 3) and the maps were subtracted from each other to create difference images (Figure 4). All the density maps were plotted using the same

arbitrary contour interval, one contour being a density value of 0.25. The average rms difference between the density maps (Table 3), i.e. the noise level in the difference maps, is approximately one contour.

In considering the projection maps and the difference images, it is important to note that the two EmrE dimers that comprise the crystallographic tetramer in the *c*222 and *p*222<sub>1</sub> crystal forms are identical, because they are related by a 2-fold symmetry axis in the plane of the membrane. In contrast, the EmrE dimers in the crystallographic tetramer in the *p*2 crystal form are different, because there is no symmetry operator relating the two. This means that there was an internal independent check for the importance of any putative differences between the images; if the same density differences were in both dimers it was likely that they were important changes, but small differences present in one dimer and not in the other were unlikely to be due to TPP<sup>+</sup> binding.

Difference images were calculated both from individual projection maps and the averaged images (Figure 4). There were some small differences between native EmrE in the *c*222 and *p*222<sub>1</sub> crystals (Figure 4(f), squares B4–G4 and B2–G2); as these EmrE molecules were expected to be the same, it indicated that density differences of three contours or less should be treated with caution when considering structural changes induced by TPP<sup>+</sup> binding. There was also a region of difference of three contours between the two *p*2 images (Figure 4(g), square C4). The average of the density

**Table 3.** Statistics of map comparisons before and after optimisation of unit cell dimensions

Projection maps being compared	Density differences after optimisation of unit cell dimensions			Density differences using original unit cell dimensions		
	rms	Max	Min	rms	Max	Min
<i>p</i> 222 <sub>1</sub> (native) minus <i>c</i> 222(native)	0.20	0.82	–0.66	0.24	0.89	–0.77
<i>p</i> 2(TPP <sup>+</sup> ):B minus <i>p</i> 2(TPP <sup>+</sup> ):A	0.16	0.86	–0.73	0.27	1.07	–1.12
<i>p</i> 2(TPP <sup>+</sup> ):A minus <i>c</i> 222(native)	0.24	1.09	–0.80	0.25	0.99	–0.91
<i>p</i> 2(TPP <sup>+</sup> ):B minus <i>c</i> 222(native)	0.27	1.30	–1.00	0.36	1.58	–1.59
<i>p</i> 2(TPP <sup>+</sup> ):A minus <i>p</i> 222 <sub>1</sub> (native)	0.26	1.11	–1.53	0.30	1.02	–1.44
<i>p</i> 2(TPP <sup>+</sup> ):B minus <i>p</i> 222 <sub>1</sub> (native)	0.27	1.26	–1.37	0.44	1.82	–1.97
Average: bound TPP <sup>+</sup> minus Average: native	0.22	1.14	–1.07	–	–	–

Density differences within the masked region are given as the root-mean-square (rms) variations in density; the maximum (max) and minimum (min) density values between the images are given. One contour in the projection map has a density value of 0.25.

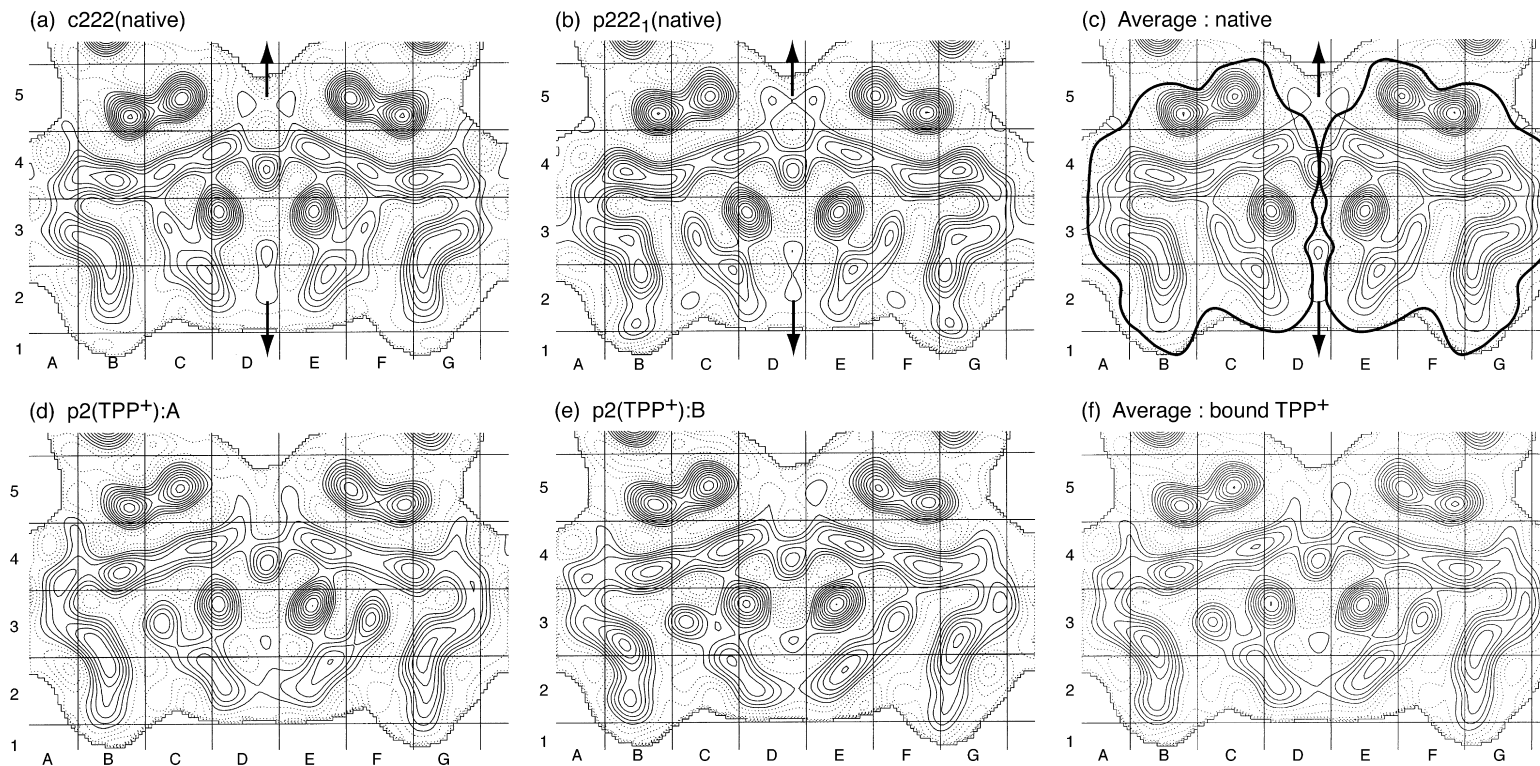


**Figure 3.** Crystallographic tetramers aligned on a grid for the generation of average images. The average native image (c) was created from merging (a) and (b) and the average EmrE image with TPP<sup>+</sup> bound (f) was created by merging (d) and (e). Arrows indicate the position of the 2-fold axis in the plane of the membrane in the *c222* and *p222*<sub>1</sub> crystal forms. The outline of the two EmrE dimers is shown in (c). The positioning of the grid does not reflect any symmetry operators. The mask used to select the areas corresponding to the crystallographic tetramer is depicted in all the images.

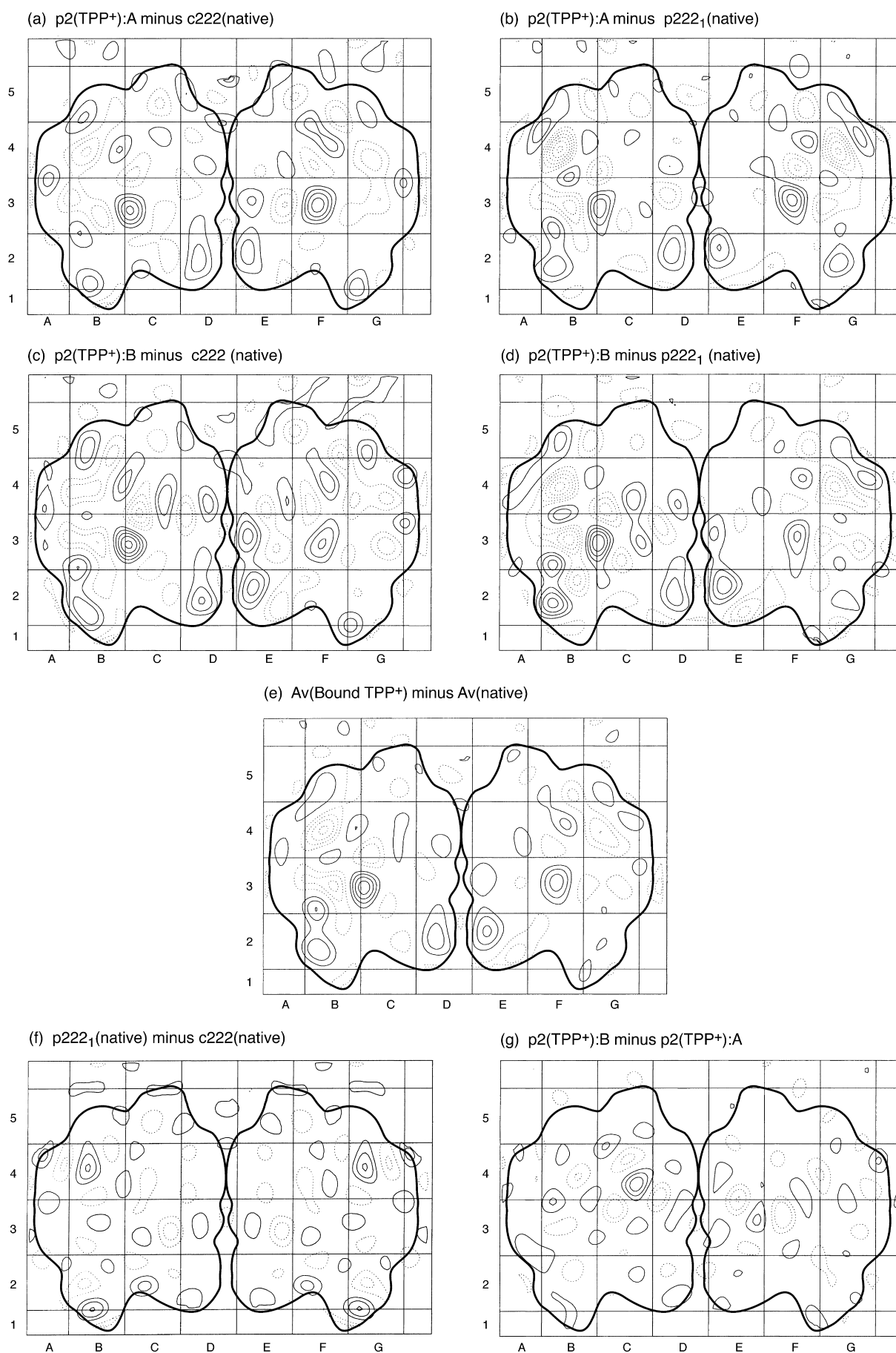


Figure 4 (legend opposite)

differences between the TPP<sup>+</sup>-bound and native EmrE projection structures (Figure 4(e)) showed two series of density differences. One series of density changes were present in all the difference images and in both the dimers of the crystallographic tetramer; the changes included the largest positive density difference of three to five contours (squares C3 and F3) and a slightly smaller positive density difference of two to three contours (squares D2 and E2). The other group of density differences were found predominantly in only one of the dimers in the crystallographic tetramer and included positive density changes of two to four contours (squares B2 and B3) and negative changes of three to six contours (squares B3, B4 and C4). Note that the depth of the negative density well in B4 coincides with the major density difference peak of three contours between the native EmrE structures (Figure 4(f)). Any interpretation of the density differences should explain satisfactorily why some density differences are in both dimers of the crystallographic tetramer and why some differences are predominantly in just one of the dimers.

#### Interpretation of density differences between native and TPP<sup>+</sup>-bound EmrE

The interpretation of the density differences was complicated because of the five possible ways that density differences could have arisen: (1) addition of extra density from TPP<sup>+</sup>; (2) conformational changes in the secondary structure of EmrE due to TPP<sup>+</sup> binding; (3) changes in the secondary structure of EmrE induced on crystallisation; (4) differences in overall tilt of EmrE in the membrane between the different crystal forms; and (5) random noise not associated with protein structural changes. Points (3)–(5) are considered here, whilst points (1) and (2) are discussed in the next section.

The average density difference image (Figure 4(e)) was overlaid onto the average native EmrE projection structure (Figure 3(c)) to highlight the regions that were apparently altered by TPP<sup>+</sup> binding (Figure 5). There were small differences in density of one contour outside the major density associated with EmrE, which was a reflection of the level of noise, suggesting that differences of more than one contour were likely to be associated with changes in EmrE structure. We did not believe that there was any difference in the relative tilt of EmrE in the membrane between the different crystal forms, because there were no consistent

density differences next to the major structural features; for instance, there were no large density differences associated with any of the three  $\alpha$ -helices nearly perpendicular to the membrane (densities labelled P in Figure 5). There was, however, a contribution in the difference density images that was probably derived from packing interactions in the *p*2 crystal that were absent from the *p*222<sub>1</sub> or *c*222 crystals. As mentioned above, the two EmrE dimers in the crystallographic tetramer in the *p*2 crystals were not related by a 2-fold in-plane symmetry axis, which implied that in projection they must be different, which was obvious from a visual inspection of the *p*2 projection maps. Why are these two dimers in the *p*2 crystals different? We did not believe that there were chemical differences between the EmrE dimers in the *p*2 crystallographic tetramer, because the crystallisation experiment contained a homogeneous population of EmrE. However, there was a significant difference in packing of the crystallographic tetramer in the *p*2 crystal compared to the *c*222 and *p*222<sub>1</sub> crystals (Figure 2). If the regions B2 and G2 (Figure 5) were considered in the context of the *c*222 and the *p*222<sub>1</sub> crystals, then it was seen that B2 and G2 were in identical environments within each crystal form. In contrast, in the *p*2 crystal form the packing of adjacent crystallographic tetramers was asymmetric (compare the packing along the unit cell *a*-axis in Figure 2(c) with the other crystal forms), which meant that B2 and G2 made different interactions with the neighbouring tetramer. This has resulted in the helix in B2 having a slightly different position, with an associated negative density adjacent to it, but there was no equivalent change in G2. The altered position of the  $\alpha$ -helix in region B2 due to asymmetric crystal contacts probably also resulted in changes to adjacent  $\alpha$ -helices, which could explain the difference in magnitude of other density differences in the arc (A) of helices compared to the other EmrE dimer (squares B2, B3 and B4). These crystal-induced conformation changes explained why we have not averaged the two EmrE dimers in the crystallographic tetramer in the difference image analysis.

#### Density differences induced by TPP<sup>+</sup> binding

After taking into consideration density differences in EmrE arising from different packing interactions between the crystallographic tetramers, there were only two regions of positive density that were associated with TPP<sup>+</sup> binding (Figure 5).

---

**Figure 4.** Difference images created from the subtraction of aligned crystallographic tetramers. Each of the projection maps depicted in Figure 3 was subtracted from each of the others to generate the difference images as described above each panel. The average difference image (e) was made from subtracting the density from the average native EmrE projection map (Figure 3(c)) from the average EmrE with TPP<sup>+</sup> bound projection map (Figure 3(f)). Contouring is on the same scale as the projection maps. The grid and EmrE dimer outlines are in exactly the same register as in Figure 3 to facilitate direct comparisons.

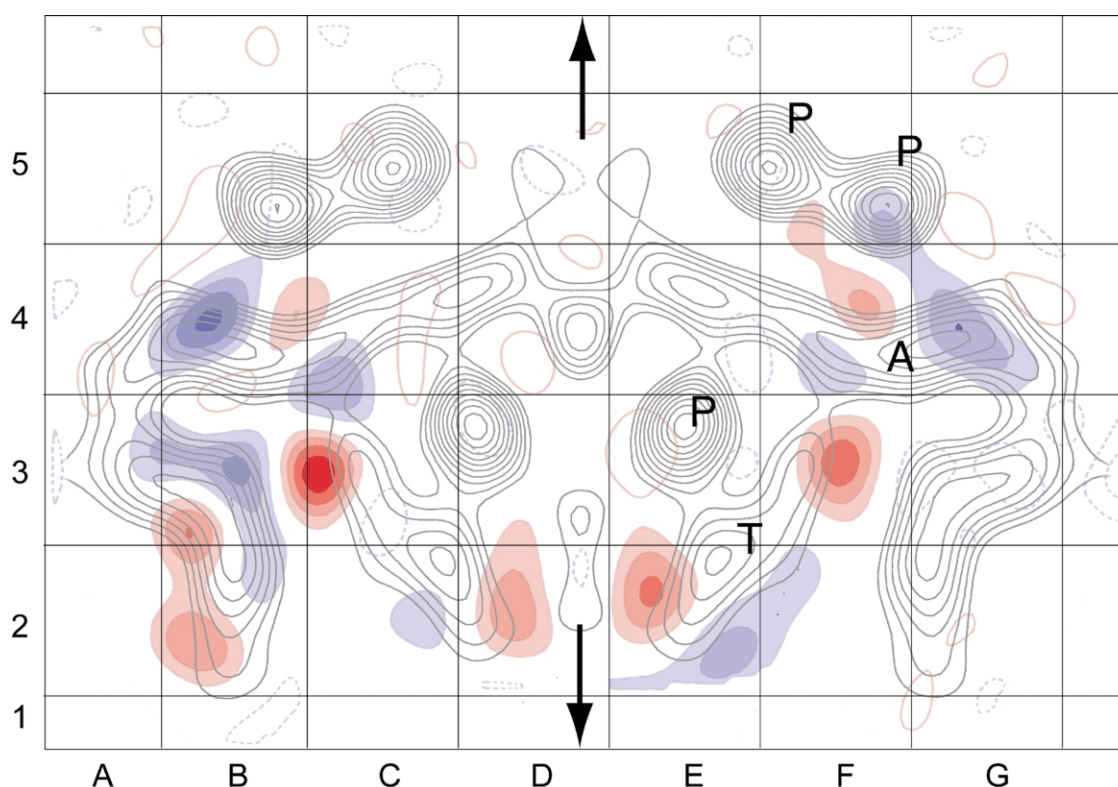


**Figure 5.** Density differences between native EmrE and EmrE with TPP<sup>+</sup> bound. The average native EmrE projection map (no substrate) from Figure 3(c) was merged with the average density difference image from Figure 4(e). Density differences are shown in either red (increase in density in crystals with TPP<sup>+</sup>) or in blue (decrease in density in crystals with TPP<sup>+</sup>). For clarity, density differences of one contour that are considered to be due to noise are not filled, but are shown as either a continuous red contour (positive density) or a broken blue line (negative density). The arrows represent the 2-fold axis in the plane of the membrane in the average native projection map, but they do not apply to the difference density. The labels on the projection map indicate the interpretation of the density previously made.<sup>6</sup> P,  $\alpha$ -helix nearly perpendicular to the plane of the membrane; A, an arc of four tilted  $\alpha$ -helices; T, a single tilted  $\alpha$ -helix. Each axis of the grid square represents 10 Å. The grid is identical with those in Figures 3 and 4.

The density peak C3–F3 was at the end of the density that represented a single tilted  $\alpha$ -helix (T). At the other end of this same helix, but on the opposite side, was the density peak D2–E2. There were two possible explanations for these peaks of density; either they represented a conformational change, i.e. the movement of part of EmrE, or they represented the addition of extra mass i.e. TPP<sup>+</sup>. From the [<sup>3</sup>H]TPP binding studies, we knew that there was one TPP<sup>+</sup> molecule bound per EmrE dimer, so it was possible that one of these peaks represented bound TPP<sup>+</sup>. We thought that the C3–F3 peak represented TPP<sup>+</sup> bound to EmrE, because there was clearly insufficient negative density adjacent to the peak to explain its presence due solely to a conformational change; this is seen most strikingly in the single difference density map in Figure 4(a). There was a consistent region of negative density (squares C4 and F4) next to the C3–F3 peak, but in the average density difference image (Figure 5) the negative density was one to two contours compared to the peak of three to four contours; this difference was above the noise level of one contour, so it was likely that there was additional density in this region, which was most probably TPP<sup>+</sup>. Given the proximity of

the C4–F4 negative density to the C3–F3 peak, it is possible that there was a small conformational change at this end of the helix that contributed to the positive density peak associated with TPP<sup>+</sup>. Another possibility is that the C3–F3 peak was caused by an increase in the order of loops between the transmembrane  $\alpha$ -helices. We think that this is unlikely, because the loops are predicted to be extremely short, given that 80% of EmrE is composed of  $\alpha$ -helices,<sup>4</sup> suggesting that the loop regions will be highly constrained in structure.

Unfortunately, it is very difficult to calculate precisely whether the density in the C3–F3 peak is sufficient to represent only TPP<sup>+</sup>. Integration of the C3 peak height and comparing it, for example, to the densities for the  $\alpha$ -helices nearly perpendicular to the membrane does not give a sufficiently accurate value, because the zero level of the projection map is the average density of the crystal as a whole, whereas the difference peak contouring starts at zero. The absolute density for the bacteriorhodopsin 2D crystal has been calculated,<sup>20</sup> but in this case, the exact lipid:protein ratio in the crystal was known. EmrE crystals contain an unknown amount of lipid, protein and detergent, and the determination of the absolute

value of each component is not trivial, especially given that a normal crystallisation contains a heterogeneous mixture of crystals, vesicles and aggregates. It is not possible to compare directly density values between the EmrE and bacteriorhodopsin projection maps because the relative scaling of contour levels is not known precisely, the zero contour being the average density. The issue is complicated because the peak is the result of TPP<sup>+</sup> binding to the protein, which must mean that it displaces something from that site, which could be lipid, detergent, water, protein side-chains or a combination of these, further complicating the calculations. A crude approximation for the density of TPP<sup>+</sup> (339 Da) would be three contours in the difference maps, assuming that an  $\alpha$ -helix nearly perpendicular to the membrane has a density of about 20 contours<sup>20</sup> and contains 20 amino acid residues with an average mass of 110 Da. This will be an overestimate of the actual value, because the difference in the electron-scattering power between TPP<sup>+</sup> and the water/protein/lipid/detergent it is replacing has not been taken into account.

The interpretation of the D2–E2 density peak is that it represents a movement of helix T, because there was negative density in squares C2–E2 that could explain the origin of the positive density. A movement of this helix would inevitably affect the packing between the EmrE dimers in the crystallographic tetramer and may explain why *p*2 crystals form, rather than crystals with *c*222 or *p*222<sub>1</sub> symmetry. The fact that *c*222 EmrE crystals change their plane group symmetry to *p*2 on addition of TPP<sup>+</sup> at pH 7 in a matter of minutes suggests that the movement of helix T is caused by TPP<sup>+</sup> binding rather than by being induced by crystal formation or by a pH effect. The juxtaposition of the D2–E2 and C3–F3 density peaks on opposite sides and ends of helix T suggests the possibility that they could both arise by a rotation of the helix about an axis perpendicular to the membrane in the middle of the helix. Given the lack of negative density in squares C3–F3 as an origin for the C3–F3 positive density difference, we feel this is unlikely. Our preferred interpretation, therefore, is that TPP<sup>+</sup> binds in the region of helix T, and causes the end of helix T to move away from the centre of the EmrE dimer; the movement of helix T alters the dimer–dimer interface in the crystallographic tetramer, thus causing the formation of *p*2 crystals rather than *c*222 or *p*222<sub>1</sub> crystals that are characteristic of native EmrE.

When the mechanism of multidrug transport is considered, there are good reasons supporting the proposal that the C3–F3 density difference represents TPP<sup>+</sup>, and that the D2–E2 density difference does not. The only residue that is absolutely required for substrate binding and transport is Glu14 in helix 1, which is predicted to be in the centre of the lipid bilayer. The fact that transport is electrogenic implies that at least two protons are required for toxin extrusion, which suggests that

the substrate is in contact with both Glu14 residues in the EmrE dimer and that proton binding to each Glu residue causes substrate release.<sup>15,16</sup> With TPP<sup>+</sup> in the centre of the dimer, there are at least four possible  $\alpha$ -helices that could be the sites of Glu14. In contrast, if the D2–E2 density represents TPP<sup>+</sup>, then only one  $\alpha$ -helix would be close enough for the site of Glu14. In this context, it must be remembered that the crystallographic tetramer would be unlikely to exist in bacteria, because each half of the tetramer would have opposite topology in the membrane.

Structural data for multidrug transporters include atomic-resolution structures of AcrB,<sup>21</sup> and the multidrug transporter homologues MsbA, a phospholipid flippase<sup>22</sup> and BtuCD, a vitamin B<sub>12</sub> transporter,<sup>23</sup> and a low-resolution structure of P-glycoprotein;<sup>24</sup> however, all these proteins are members of superfamilies different from that of EmrE and they are thus structurally unrelated to EmrE. There is a striking difference between the large conformation changes seen in P-glycoprotein during its transport cycle<sup>24</sup> and the relatively small changes seen for substrate binding to EmrE. The positive identification of substrate-binding pockets has not been reported, but the above structures all contain vestibules in the centres of the oligomeric assemblies that were proposed to be part of the substrate translocation pathways. The finding that the substrate for EmrE probably binds at the monomer–monomer interface in the centre of the dimer supports the view that transport through multidrug transporters occurs in the centre of the protein. Mechanistic studies on substrate transport by the bacterial multidrug transporters AcrB<sup>25</sup> and LmrA<sup>26</sup> suggest that substrates are bound from the inner leaflet of the cytoplasmic membrane and extruded into either the outer leaflet or directly into the external aqueous medium. This implies that if transport occurs through the centre of the oligomer, then there must be a pathway from the lipid bilayer into the protein. The transporters mentioned above are unrelated to EmrE, but it seems likely that, because of the similarity in the hydrophobic nature of EmrE substrates compared to those of other multidrug transporters, EmrE may bind substrates from the inner leaflet of the cytoplasmic membrane. Determination of whether there is a direct route for TPP<sup>+</sup> from the lipid bilayer into the centre of the transporter will have to await further data from 3D reconstructions of EmrE from the 2D crystals.

## Materials and Methods

### EmrE purification

EmrE was expressed and purified as described.<sup>6</sup> Briefly, EmrE was solubilized from *E. coli* membranes with dodecylmaltoside (DDM; Glycon, Germany) and purified using the His<sub>6</sub> tag at the C terminus on a Ni<sup>2+</sup> affinity column (Qiagen). The eluted protein was further

purified on a gel-filtration column (Superdex 200, Amersham Pharmacia) and an anion-exchange column (PI resin, Poros). EmrE was concentrated using a 30 kDa cut-off concentrator (Centriprep, Amicon). Protein concentration was determined by an amido black protein assay,<sup>27</sup> which includes a protein precipitation step to ensure there was no interference in the assay by lipids, detergents or buffers. The actual protein concentration was determined by amino acid analysis. A factor of 1.34 was required to convert the apparent EmrE concentration determined from the protein assay to the actual protein concentration determined by amino acid analysis.

### [<sup>3</sup>H]TPP<sup>+</sup> binding assays

[<sup>3</sup>H]TPP<sup>+</sup> binding assays were performed on the purified EmrE solubilized in DDM. Binding assays were started by the addition of [<sup>3</sup>H]TPP<sup>+</sup> (Amersham Pharmacia) to the EmrE sample (120  $\mu$ l final volume in 20 mM Tris-HCl (pH 8), 100 mM NaCl, 0.1% (w/v) DDM) and incubated on ice for one hour. Spin columns were made for each assay point from Sephadex G25 medium (Amersham Pharmacia) pre-equilibrated in 20 mM Tris-HCl (pH 8.0), 150 mM NaCl, 0.1% DDM. Each column contained 2.4 ml of packed Sephadex in 6 ml Quik-Sep disposable polypropylene columns (Advanced Laboratory Techniques, UK) and was pre-spun (three minutes, 240g); 50–80  $\mu$ l of sample was loaded per column, which was then spun into a scintillation vial (four minutes, 330g). The amount of <sup>3</sup>H in the sample was determined by scintillation counting. Background binding of [<sup>3</sup>H]TPP<sup>+</sup> was determined by the addition of 100  $\mu$ M TPP<sup>+</sup> to the assay for low [<sup>3</sup>H]TPP<sup>+</sup> concentrations (nM); apparent non-specific binding was about 0.5–1% of specific binding at 180 nM TPP<sup>+</sup>, which was due to some unbound [<sup>3</sup>H]TPP<sup>+</sup> not being retained by the gel-filtration column. At very high concentrations of [<sup>3</sup>H]TPP<sup>+</sup>, a 1000-fold excess of cold TPP<sup>+</sup> was impossible to achieve, so background was equated to the amount of TPP<sup>+</sup> that eluted from the spin column in the absence of EmrE. Binding analyses were performed by non-linear regression using Graphpad Prism2.0.

### Crystallisation and electron microscopy

The 2D crystallisation of EmrE was performed by dialysis for 10–14 days exactly as described<sup>6</sup> on addition of dimyristoylphosphatidylcholine, using a final concentration of 0.5–1 mg/ml of EmrE. The crystals that had *c*222 symmetry were grown by dialysis against 20 mM sodium phosphate (pH 7.0), 100 mM NaCl, 2 mM MgCl<sub>2</sub>, 1 mM EDTA, 4 mM DTT, 4 mM 2-mercaptoethanol, 10 mM sodium azide; the *p*2 crystals were grown in the same buffer, except that the pH was 7.5 and that 20  $\mu$ M TPP<sup>+</sup> was present. Crystals were placed on four day-old carbon-coated electron microscopy grids, blotted and plunged into liquid ethane. Samples were loaded onto a liquid nitrogen-cooled Gatan 626 cryo-stage and analysed by standard low-dose cryo-EM techniques (10–15e  $\text{\AA}^{-2}$ ) on a Technai F30 electron microscope at an accelerating voltage of 300 keV. Images were collected with flood beam illumination at a magnification of 56,000 $\times$ . The quality of the crystals on each image was assessed by optical diffraction and the best images were digitised using a Zeiss SCAI scanner using a 7  $\mu$ m step size. Image processing was performed using the MRC package as described.<sup>6</sup>

### Construction of difference maps

The aim was to compare the projection maps objectively to maximise the signal to noise ratio. Superposition of the initial maps showed that the effect of small errors in cell dimensions would overwhelm the real differences between the structures if the maps were just subtracted from each other. There is always uncertainty in the magnification of electron micrographs and errors in the determination of cell dimensions of a few percentage points are not unlikely. Therefore, before detailed comparisons could be made it was necessary to standardise the relative cell dimensions. One set of cell dimensions was chosen to remain unaltered (that of the *c*222 form), whilst those of the three other forms (*p*222<sub>1</sub>, *p*2:A and *p*2:B) were adjusted so as to minimise the differences between the maps. Once the differences between the maps had been minimised, any remaining differences above the noise level between the forms with and without bound TPP would be associated with the binding of substrate.

To allow superimposition of the projection maps, the origin for a common orientation of the crystallographic tetramer was selected as the 2-fold axis perpendicular to the membrane between the four apparently vertical helices in the middle of the tetramers coloured blue in Figure 2. The common orientation was defined by a new *y*-axis through this origin and parallel with the two rows of (blue) tetramers. As the packing of the proteins within the two rows of tetramers was apparently identical in all forms, the cell dimension parallel with these rows was assumed to be identical. The dimension of the *c*222 form in this direction is 72.5  $\text{\AA}$ . In the first stage of cell dimension standardisation, the corresponding dimension in each of the three other forms was also set to 72.5  $\text{\AA}$ , and the remaining cell dimension was altered in proportion (Table 2). Maps were calculated for the four forms in the common orientation with the adjusted cell dimensions, and difference images between them were calculated. The rms density difference between two maps was used as a measure of the correctness of the relative cell dimensions, which necessitated the use of a mask to remove contributions from differences outside the region of common packing. A mask was produced from the correlation maps between pairs of maps, all of which looked very similar; the region of common packing had correlation  $\geq 0.5$  and outside this region, where interactions between pairs of rows differed, the correlation was  $< 0.5$ . The mask was used in all further calculations to delineate the areas of maps that were to be compared.

The next step was to optimise the second cell dimension. This was necessary because the *a*-axis/*b*-axis ratio for the individual images within each space group was not constant, probably due to small tilts of the specimen. It was also necessary to consider the relative scaling between the projection maps, because each initial Fourier map had been calculated with the maximum density set arbitrarily to 2.5, which was not necessarily optimum for relative scaling between maps. Comparisons were made of the *c*222 crystal form with each of the three others by altering the second dimension around the 72.5 value (Table 1) in 1  $\text{\AA}$  steps, and subsequently in finer steps, until the rms deviation between the maps was minimised. The scale factor was optimised in a similar fashion. The consistency between other pairwise comparisons was sufficiently good to enable a choice of optimum cell dimensions and scale factors (Table 3). The

four masked re-oriented maps (Figure 3) and their averages were calculated using the optimised cell dimensions and scale factors listed in Table 2, and difference images between these final maps were determined (Figure 4).

To assess the improvement in signal to noise ratio achieved by the adjustment of cell dimensions, difference images within the masked area were calculated using the experimental cell dimensions. The statistics of these experimental maps are included in Table 3 for comparison with the final statistics. The adjustment of the cell dimensions resulted in a decrease in the rms difference within the masked region in all comparisons. The remaining noise is approximately one contour level, as plotted in the maps.

Use was made of several programs in the CCP4 programme suite.<sup>28</sup> Fourier maps were calculated using FFTBIG and EXTEND. All other programs used cannot work with a projection map, so 3D maps were calculated with two sections perpendicular to the z-axis, each section being identical with the projection map. Maps were plotted using NPO. The maps were brought to a common origin, orientation and extent using MAPROT in mode FROM, with rotation/translation parameters derived from inspection of the original maps. MTZUTILS was used to effect cell dimension changes where necessary. The correlation between two maps was calculated using MAPROT in mode CORR. MAPMASK was used with option CUT 0.5 to create a mask.map file from a correlation map. The area with correlation  $\geq 0.5$  was included in the mask. MAPROT was then used with mask.map as the file for mskin, to produce maps in the common orientation but masking out the density outside the common region. Difference images between pairs of maps were calculated with OVERLAPMAP, with application of scale factors if necessary. Scripts for comparison of maps in pairs were set up that enabled easy assessment of improvement in cell dimension and scale factor. The optimum values for cell dimensions and scale factors were selected by inspection of the statistics of the various comparisons.

## Acknowledgements

We are indebted to R. Henderson for help and advice throughout this work, and for the support and comments from S. Schuldiner. We are grateful to D. Owen for performing amino acid analyses on purified EmrE and J. Berriman for advice on electron microscopy. I.U.-B. was funded by a European Molecular Biology Organisation Long-Term Fellowship.

## References

- Zgurskaya, H. I. & Nikaido, H. (2002). Mechanistic parallels in bacterial and human multidrug efflux transporters. *Curr. Protein Pept. Sci.* **3**, 531–540.
- Paulsen, I. T., Skurray, R. A., Tam, R., Saier, M. H., Jr, Turner, R. J., Weiner, J. H. *et al.* (1996). The SMR family: a novel family of multidrug efflux proteins involved with the efflux of lipophilic drugs. *Mol. Microbiol.* **19**, 1167–1175.
- Schuldiner, S., Granot, D., Mordoch, S. S., Ninio, S., Rotem, D., Soskin, M. *et al.* (2001). Small is mighty: EmrE, a multidrug transporter as an experimental paradigm. *News Physiol. Sci.* **16**, 130–134.
- Arkin, I. T., Russ, W. P., Lebendiker, M. & Schuldiner, S. (1996). Determining the secondary structure and orientation of EmrE, a multi-drug transporter, indicates a transmembrane four-helix bundle. *Biochemistry*, **35**, 7233–7238.
- Schwaiger, M., Lebendiker, M., Yerushalmi, H., Coles, M., Groger, A., Schwarz, C. *et al.* (1998). NMR investigation of the multidrug transporter EmrE, an integral membrane protein. *Eur. J. Biochem.* **254**, 610–619.
- Tate, C. G., Kunji, E. R., Lebendiker, M. & Schuldiner, S. (2001). The projection structure of EmrE, a proton-linked multidrug transporter from *Escherichia coli*, at 7 Å resolution. *EMBO J.* **20**, 77–81.
- Yerushalmi, H., Lebendiker, M. & Schuldiner, S. (1996). Negative dominance studies demonstrate the oligomeric structure of EmrE, a multidrug antiporter from *Escherichia coli*. *J. Biol. Chem.* **271**, 31044–31048.
- Muth, T. R. & Schuldiner, S. (2000). A membrane-embedded glutamate is required for ligand binding to the multidrug transporter EmrE. *EMBO J.* **19**, 234–240.
- Rotem, D., Sal-man, N. & Schuldiner, S. (2001). *In vitro* monomer swapping in EmrE, a multidrug transporter from *Escherichia coli*, reveals that the oligomer is the functional unit. *J. Biol. Chem.* **276**, 48243–48249.
- Soskine, M., Steiner-Mordoch, S. & Schuldiner, S. (2002). Crosslinking of membrane-embedded cysteines reveals contact points in the EmrE oligomer. *Proc. Natl Acad. Sci. USA*, **99**, 12043–12048.
- Yerushalmi, H., Lebendiker, M. & Schuldiner, S. (1995). EmrE, an *Escherichia coli* 12-kDa multidrug transporter, exchanges toxic cations and H<sup>+</sup> and is soluble in organic solvents. *J. Biol. Chem.* **270**, 6856–6863.
- Grinius, L. L. & Goldberg, E. B. (1994). Bacterial multidrug resistance is due to a single membrane protein which functions as a drug pump. *J. Biol. Chem.* **269**, 29998–30004.
- Yerushalmi, H. & Schuldiner, S. (2000). An essential glutamyl residue in EmrE, a multidrug antiporter from *Escherichia coli*. *J. Biol. Chem.* **275**, 5264–5269.
- Yerushalmi, H., Mordoch, S. S. & Schuldiner, S. (2001). A single carboxyl mutant of the multidrug transporter EmrE is fully functional. *J. Biol. Chem.* **276**, 12744–12748.
- Yerushalmi, H. & Schuldiner, S. (2000). A common binding site for substrates and protons in EmrE, an ion-coupled multidrug transporter. *FEBS Letters*, **476**, 93–97.
- Yerushalmi, H. & Schuldiner, S. (2000). A model for coupling of H(+) and substrate fluxes based on “time-sharing” of a common binding site. *Biochemistry*, **39**, 14711–14719.
- Lebendiker, M. & Schuldiner, S. (1996). Identification of residues in the translocation pathway of EmrE, a multidrug antiporter from *Escherichia coli*. *J. Biol. Chem.* **271**, 21193–21199.
- Mordoch, S. S., Granot, D., Lebendiker, M. & Schuldiner, S. (1999). Scanning cysteine accessibility of EmrE, an H<sup>+</sup>-coupled multidrug transporter from *Escherichia coli*, reveals a hydrophobic pathway for solutes. *J. Biol. Chem.* **274**, 19480–19486.
- Subramaniam, S., Lindahl, M., Bullough, P., Faruqi, A. R., Tittor, J., Oesterhelt, D. *et al.* (1999). Protein

- conformational changes in the bacteriorhodopsin photocycle. *J. Mol. Biol.* **287**, 145–161.
20. Engelman, D. M., Henderson, R., McLachlan, A. D. & Wallace, B. A. (1980). Path of the polypeptide in bacteriorhodopsin. *Proc. Natl Acad. Sci. USA*, **77**, 2023–2027.
  21. Murakami, S., Nakashima, R., Yamashita, E. & Yamaguchi, A. (2002). Crystal structure of bacterial multidrug efflux transporter AcrB. *Nature*, **419**, 587–593.
  22. Chang, G. & Roth, C. B. (2001). Structure of MsbA from *E. coli*: a homolog of the multidrug resistance ATP binding cassette (ABC) transporters. *Science*, **293**, 1793–1800.
  23. Locher, K. P., Lee, A. T. & Rees, D. C. (2002). The *E. coli* BtuCD structure: a framework for ABC transporter architecture and mechanism. *Science*, **296**, 1091–1098.
  24. Rosenberg, M. F., Velarde, G., Ford, R. C., Martin, C., Berridge, G., Kerr, I. D. *et al.* (2001). Repacking of the transmembrane domains of P-glycoprotein during the transport ATPase cycle. *EMBO J.* **20**, 5615–5625.
  25. Zgurskaya, H. I. & Nikaido, H. (1999). Bypassing the periplasm: reconstitution of the AcrAB multidrug efflux pump of *Escherichia coli*. *Proc. Natl Acad. Sci. USA*, **96**, 7190–7195.
  26. Margolles, A., Putman, M., van Veen, H. W. & Konings, W. N. (1999). The purified and functionally reconstituted multidrug transporter LmrA of *Lactococcus lactis* mediates the transbilayer movement of specific fluorescent phospholipids. *Biochemistry*, **38**, 16298–16306.
  27. Schaffner, W. & Weissmann, C. (1973). A rapid, sensitive, and specific method for the determination of protein in dilute solution. *Anal. Biochem.* **56**, 502–514.
  28. Collaborative Computational Project, Number 4 (1994). The CCP4 suite: programs for protein crystallography. *Acta Crystallog. sect. D*, **50**, 760–763.

*Edited by W. Baumeister*

*(Received 25 April 2003; received in revised form 30 June 2003; accepted 2 July 2003)*